



The University of Manchester
School of Physics and Astronomy

Self Similarity of Large Galaxy Structures using the MACSIS Hydrodynamical Simulations

William Cooper^{*}
MPhys Project

Supervisor: Dr Scott Kay
Project collaborator: Aaron Callaghan

(Dated: May, 2023)

In a Λ -Cold-Dark-Matter Universe, massive galaxy clusters form primarily through hierarchical structure formation. Under the simplest model, only non-linear processes occur during the formation of clusters. Therefore, they can be said to be scaled versions of each other, known as being self-similar. In this paper, the MAssive ClusterS and Intercluster Structures (MACSIS) N-body hydrodynamical simulation provides a sample of 390 Massive clusters with abundant substructures to search for evidence of self-similar evolution. The hot X-ray emitting Intra-Cluster-Medium (ICM) is of interest in this paper as our results will be comparable to X-ray observations. Normalised median ICM density, pressure and temperature radial profiles are plotted ($0.12 \leq R/R_{200} \leq 1.7$) for three mass bins representing galaxy groups, clusters and massive clusters across a range of redshifts ($0 \leq z \leq 3$). This is to investigate the effect mass has on non-gravitational processes and, by extent, self-similar evolution. An obvious trend of increasing dark matter halo mass with increased self-similarity is found. The shallower gravitational potential well of lower mass haloes, such as groups, cannot suppress the increase of feedback with decreasing redshift, inducing a deviation away from self-similarity. A case study of a merging MACSIS cluster was found to produce a shock front disrupting and heating the ICM and negatively affecting that cluster's self-similar behaviour. The ICM can inverse Compton scatter Cosmic Microwave Background (CMB) photons giving rise to the Sunyaev-Zeldovich (SZ) effect. This provides an alternate observation method to X-rays, and in principle, it is independent of redshift, making it ideal for studying high redshift clusters, known as protoclusters. We attempted to produce some observationally realistic SZ maps. Inspired by previous work, substructures beyond the Friends-of-Friends (FoF) algorithm were found and analysed using SUBFIND. The number of subhaloes resolved at $z = 0$ doubled the number of FoF haloes showing how much substructure is missing by only utilising FoF. However, by plotting the baryon fraction of the subhaloes, some low-mass haloes overestimate the baryon fraction. Overall, our radial profiles are consistent with X-ray observations and other simulations. The SZ maps built a good foundation for future work on creating observationally realistic maps, and with stricter selection criteria on subhaloes, they could be incorporated into future work.

^{*} will.coops@me.com

I. INTRODUCTION

Galaxies in the Universe are not uniformly scattered; a significant fraction in this epoch currently reside in Large Scale Structures (LSS). LSS consist of groups, clusters and massive clusters; hereafter, clusters will be used to generalize large dark matter haloes unless specifically specified.

Clusters situate at nodes of the cosmic web (Coil 2013; Dickinson et al. 2019; Mo, C., et al. 2010). The cosmic web formed through primordial quantum density perturbations, present in the very early Universe, enhanced by gravity during the inflation stage of the Universe (Dickinson et al. 2019; Poudel, A. et al. 2017). These perturbations are observed via temperature fluctuations in the Cosmic Microwave Background (CMB) (A. A. Vikhlinin et al. 2014). These perturbations, over cosmic time, enlarge enough that they collapse under their own gravity to form virialised regions known as dark matter haloes (Barnes, Kay, et al. 2016). However, the galaxies observed are not entirely dark matter haloes; they contain baryons which have cooled and condensed to form galaxies inside the dark matter halo's potential well (White et al. 1978; Dickinson et al. 2019; Poudel, A. et al. 2017). Therefore, all galaxies and clusters are known to be embedded in extensive distributions of cold dark matter (Taylor 2011). These dark matter haloes grow by accreting mass from their surroundings or primarily by hierarchical structure formation under the cosmological model Λ CDM. This consists of mergers with other dark matter haloes to form small-scale structures, which subsequently merge to form clusters, hence a hierarchy (Diemand et al. 2011a; Castiblanco et al. 2019; Poudel, A. et al. 2017). A cluster is thought to have merged several times over its lifetime, building up an anisotropic structure that retains a thermal and dynamical footprint of older structures (Dressler et al. 1988). Furthermore, given that the dynamical timescales of clusters are similar to the Universe's age, they reserve a footprint of their formation (Mushotzky 1998).

The Λ -Cold Dark Matter (Λ CDM) model is regarded as the 'standard' cosmological model due to its success in explaining the CMB and hierarchical structure formation. A cosmological model describes the evolution and structure of the Universe (Ellis 2006; Diemand et al. 2011b). The Λ CDM model represents a flat Universe and suggests the Universe is composed of 3 elements: baryonic matter, which only represents a small fraction of the total mass and two dominant dark components, Cold Dark Matter(CDM) and dark energy(Λ). Collectively this yields the appropriate cosmological parameters needed to simulate hierarchical structure formation at the current epoch (Taylor 2011; Huss et al. 1999). Simula-

tions like MACSIS use Λ CDM cosmology to create realistic clusters.

The MAssive ClusterS and Intercluster Structures (MACSIS) project is an N-body, zoom simulation of 390 massive galaxy clusters reaching up to $10^{15.6}$ solar masses. The clusters are sampled from a large $3.2Gpc^3$ dark matter parent simulation at $z = 0$, which is then re-simulated with full baryonic gas physics to allow self-consistent observable predictions (Barnes, Kay, et al. 2016; Cooper et al. 2022). The MACSIS project has been developed by Barnes, Kay, et al. (2016), utilising a Particle-Mesh (PM) algorithm in conjunction with a hierarchical Tree algorithm, collectively known as TreePM (Bagla 2002).

Previous work (Cooper et al. 2022) focused on the redshift evolution of baryon content of galaxy groups and clusters. A strong correlation between mass and baryon fraction was found alongside the trend of decreasing baryon fraction with decreasing redshift. Lower-mass dark matter haloes also lost baryonic matter more rapidly than higher-mass haloes. This is in agreement with real-world observations and other simulations. The cause can be narrowed down to the shallower gravitational potential wells of low-mass haloes allowing feedback processes to push out the baryonic matter more efficiently. A candidate catalogue was created and became the foundation of that project. A was candidate is defined as all structures found by the friends-of-friends (FoF) algorithm in every cluster for every redshift, and in this paper, we will refer to them as FoF haloes. This catalogue is also the foundation of this project and is used for most of our analysis.

Our previous work heavily influences this paper's investigation of substructures beyond the FoF haloes. This comes from missing apparent structure from mass maps created. However, the primary objective of this paper is to investigate high redshift dark matter haloes to make observable predictions and search for self-similarity. Current observational techniques of clusters include X-ray and Sunyaev-Zeldovich effect studies. These can be replicated in hydrodynamic simulations by selecting only hot gas particles representing the Intra-Cluster-Medium (ICM). The redshift evolution of the ICM inside groups, clusters and massive clusters is analysed using radial profiles that are compared across a range of redshift, $0 \leq z \leq 3$, to reveal evidence for self-similar evolution. In the (strong) self-similar model, all dark matter haloes, scaled by their mass, are identical objects. The hot gas density, thermal pressure, and temperature profiles have the redshift and mass dependence removed by normalizing them by their virial counterparts computed by the self-similar model (Bower 1997; F. Pearce 2020; Short et al. 2010).

This paper is organised as follows. Section II further explains

large structures and categorises them for later analysis alongside the theory behind observational techniques to study them. Moreover, the algorithms and code behind the MACSIS simulation are discussed. Section III briefly investigates substructures found by the SUBFIND algorithm. The penultimate section IV uses radial profiles to reveal self-similarity within the evolution of groups, clusters, and massive clusters. Finally, section V uses the thermal Sunyaev-Zeldovich effect and smoothing techniques to convert projected thermal pressure maps into observationally realistic maps.

II. THEORY AND SIMULATIONS

This section distinguishes between different mass dark matter haloes, so in section IV, the effect halo mass has on self-similarity can be investigated. The Λ CDM model and virilisation are discussed to understand the origin of clusters, through mergers investigated in IV D, and what properties we can use to study them. The selection of MACSIS clusters is described alongside how the relevant physics processes are simulated using embedded algorithms. Additionally, the under-laying physics of X-rays and the Sunyaev-Zeldovich effect observations are described to support sections IV and V, respectively.

A. Large Scale Structures

The Universe demonstrates an abundance of structures spanning various cosmological scales. Large Scale Structures (LSS) are defined as the inhomogeneous distribution of galaxies on scales larger than a galaxy that traverse a significant fraction of the observable Universe. LSS can be classified into voids, filaments, massive clusters, clusters, and groups, presented in descending size (Poudel, A. et al. 2017; Coil 2013; Tully et al. 2014). We are interested in the latter three as they are the easiest to observe with methods such as the Sunyaev-Zeldovich effect and X-ray studies and can be used to trace mass distribution on large scales. Nevertheless, filamentary structures dominate the cosmic web; they act as massive linked bridges between clusters at the nodes of the cosmic web that play a significant role in their evolution by funnelling galaxies and dark matter, as found in Poudel, A. et al. (2017). Almost half of all galaxies and mass in the observable Universe reside in cosmic filaments. However, voids are the largest-scale structures in the observable Universe. They are vast regions of relatively empty space, containing very few galaxies, filling the remaining space of the cosmic web (Coil 2013; Dickinson et al. 2019; Poudel, A. et al. 2017;

Coil 2013; Tully et al. 2014). Galaxy redshift surveys, such as Colless et al. (2001), clearly exhibit the structure of the cosmic web and LSS. A galaxy redshift survey measures the distance to individual galaxies by using the Doppler shift of emitted radiation from them. The aforementioned survey studied relatively close galaxies with a median depth of $z = 0.11$; however, even at this scale, an inhomogeneous structure is apparent.

B. Λ CDM and Virialization

The Λ CDM model models a flat, accelerating universe driven by dark energy (Λ). From the Planck Collaboration et al. (2014), the characteristic cosmological parameters for the Λ CDM model are $\Omega_b = 0.04825$, $\Omega_m = 0.307$, $\Omega_\Lambda = 0.693$, and $h = 0.6777$. Note these parameters are the values used in MACSIS, which are not the exact same (Barnes, Kay, et al. 2016). The expansion of the Universe is parameterized by the dimensionless scale factor

$$a = \frac{1}{1+z}, \quad (1)$$

where z is the observed redshift. The critical density of the Universe is the average energy density required for a flat Universe. Therefore, the background density (ρ_b) can be approximated to be the critical density for Λ CDM cosmology. The present-day critical density ($\rho_{cr,0}$) can be written as

$$\rho_{cr,0} = \frac{3H_0}{8\pi G}, \quad (2)$$

where $H_0 = 100h[kms^{-1}Mpc^{-1}]$ is the present-day Hubble parameter, h is the dimensionless Hubble parameter and G is the gravitational constant. However, for an expanding Universe, it is obvious to infer it was denser at greater redshift. Therefore, the redshift dependant Λ CDM critical density is as follows

$$\rho_{cr}(z) = \rho_{cr,0}E^2, \quad (3)$$

where

$$E = \sqrt{\Omega_m a^{-3} + \Omega_\Lambda}. \quad (4)$$

Variable a is from equation 1, and the mass and dark energy fraction parameters are Ω_m and Ω_Λ , respectively. We can assume $\Omega_\Lambda = 1 - \Omega_m$ as this equation is an adaptation of Friedman's equation where the radiation parameter Ω_r is negligible and the curvature parameter $\Omega_k = 0$ as Λ CDM represents a flat Universe. These derivations follow Coles et al. (2002), Liddle et al. (2000), and Mo, Bosch, et al. (2010).

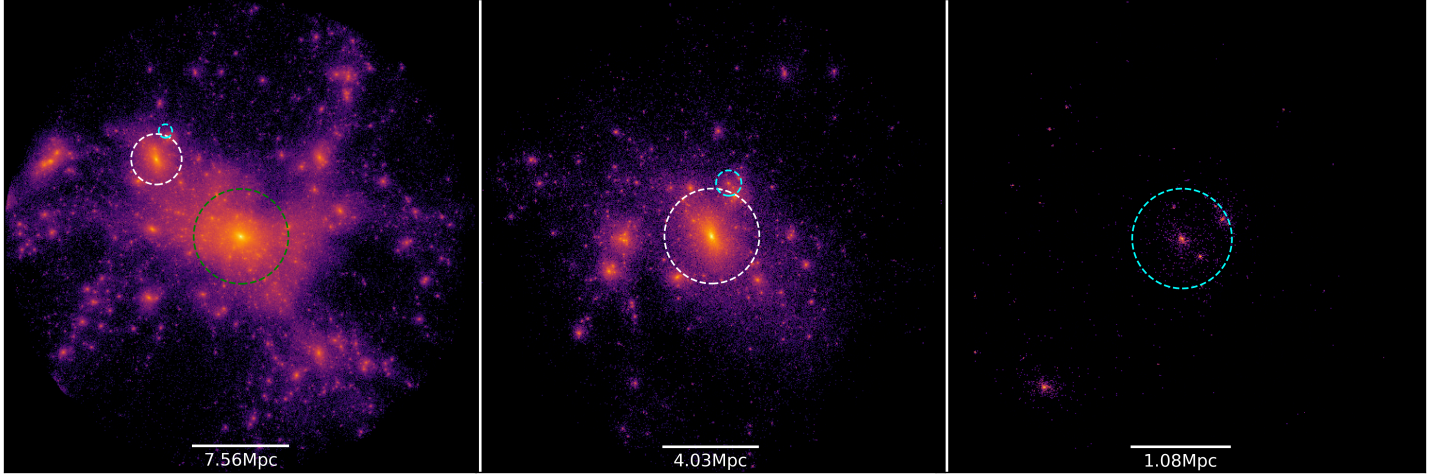


FIG. 1: Illustration of different mass dark matter haloes from MACSIS halo 0, at $z = 0$. Using our mass classification defined in table I, the left image shows a massive galaxy cluster (green), the middle a galaxy cluster (white), and the left is a galaxy group (red). The plot is a 2D histogram of dark matter in the x-z plane. The dashed rings are plotted at the centre of the potential of the halo with radius R_{200} , with the scale specified at the bottom. The colour of the dashed rings distinguishes the haloes, all of which can be located in the left image. Each region plotted extends to that structure's $5R_{200}$.

As briefly mentioned in section I, in Λ CDM cosmology, dark matter is responsible for the formation of LSS. The primordial perturbations, in the otherwise homogeneous Universe, contained a universal fraction of baryons and dark matter. When the perturbation collapses under its own gravity, the collisionless dark matter rapidly relaxes to form dark matter haloes, whilst the baryonic gas is shocked to the virial temperature and settles into hydrostatic equilibrium with the potential well of the dark matter halo (Mo, Bosch, et al. 2010; Poudel, A. et al. 2017).

When calculating a cluster's mass, we assume spherical symmetry and virial equilibrium, $2K + U = 0$, where K is the kinetic energy and U is potential energy. Using the Spherical Top-Hat Collapse Model (STHCM), it can be shown for Λ CDM cosmology, the density of a virialized halo, such as a galaxy, is roughly 178 times the background density which we assumed to be the critical density above. Given the approximations made in the STHCM an overdensity of $\Delta_c = \frac{\rho}{\rho_b(z)} = 200$ is used. Now we can write our mean density (ρ) of a virialized sphere as

$$M_{\Delta_c} = \Delta_c \rho_{cr}(z) \frac{4}{3} \pi (R_{\Delta_c})^3. \quad (5)$$

When the overdensity $\Delta_c = 200$, the virial mass and radius are M_{200} and R_{200} respectively and ρ_{cr} is the same as equation 3. This equation is very important as it relates an easily observable value R_{200} to a fundamental but unobservable property M_{200} .

C. Galaxy Structure Classification

Under hierarchical structure formation, smaller haloes merge to form larger haloes of dark matter. As the universe continued to expand, baryons cooled and collapsed into the potential well of the dark matter haloes forming the first galaxies. These galaxies continuously merge, creating larger structures, such as groups, clusters and ultimately, massive clusters. Large structure form last from the successive merging of smaller structures. Dark matter haloes can be classified by their mass, radius and galaxies bound to them. However, there is no standard characterisation for groups, clusters and massive clusters, only a rough outline. The specific mass limits we place are shown in table I below.

TABLE I: Galaxy mass classification

	Groups	Clusters	Massive Clusters
Mass(M_{200})	$10^{13} - 10^{14}$	$10^{14} - 10^{15}$	$\geq 10^{15}$
Galaxies(#)	10	100	1000

The mass is the only boundary used in this paper to separate the galaxy structures; other information in the table is solely there to show what is expected. Using figure 1 the clear distinction between the scale and structure of groups, clusters and massive clusters can be seen. This example exemplifies how the massive cluster sits at the centre, with clusters contained in filaments being funnelled towards it and a group merging with the cluster simultaneously. Collectively this visually shows the idea of hierarchical structure formation.

D. MACSIS

Cosmological simulations are important in the theoretical studies of structure formation. N-body simulations can calculate gravitational and hydro-dynamical interactions between point-like particles. Particles in N-body simulations act as mass traces, namely for dark matter, gas and stars for MACSIS. To produce a substantial population of massive galaxy clusters, a large-volume N-body simulation is required. However, simulating a volume on this scale with full hydrodynamic and gas physics is too computationally expensive. Therefore, a parent simulation is run using a cold dark-matter-only N-body simulation as it is a collisionless fluid meaning it only interacts gravitationally and can be modelled using the collisionless Boltzmann equation (Davis et al. 1985). However, it is known that non-gravitational processes, such as feedback, play a crucial role in the formation of galaxy structure, see Planelles, Schleicher, et al. (2014) and Sijacki et al. (2007). The GAlaxies with Dark matter and Gas intEraCt (GADGET) code solves this problem by evolving the self-gravitating collisionless dark matter fluid using the N-body method and a collisional ideal gas using Smoothed Particle Hydrodynamics (SPH). GADGET was introduced in Springel, Yoshida, et al. (2001) and most recently reviewed by Springel (2005).

Gravitational forces are computed by a hierarchical multipole expansion in the form of a Tree Particle-Mesh (TreePM) algorithm. The PM method calculates long-range forces by smoothing the point-like particle distribution onto a grid and solving with Fourier techniques. The short-range forces are calculated using a tree method. The tree method divides the volume of the simulation into eight equal-volume cubes. A hierarchical mesh tree is constructed by recursively subdividing each cube into eight smaller cubes until every particle is in its own sub-cube. TreePM employs the best of both algorithms to most efficiently and accurately calculate gravitational forces. Hydrodynamics are calculated with SPH; it uses a set of tracer particles to describe the state of a fluid, with continuous fluid quantities being defined by a kernel interpolation technique.

The parent simulation was run with $N = 2520^3$ dark matter particles initially arranged in a glass configuration. The simulation was then evolved from $z = 127$ using the hybrid Lagrangian TreePM-SPH code from GADGET3 (Barnes, Kay, et al. 2016; Springel, Yoshida, et al. 2001; Springel 2005).

Haloes were identified in the parent simulation at $z = 0$ using the Friends-of-Friends algorithm (Davis et al. 1985). The algorithm links particles closer than the linking length $b = 0.2$, set by Barnes, Kay, et al. (2016), to create a network

of particles representing a virialized dark matter halo. Haloes found by FoF will be called *FoF haloes* henceforth. The MACSIS sample used in this paper were 390 FoF haloes selected from logarithmically spaced bins over the mass range, $10^{15} \leq M_{FoF} \leq 10^{15.6}$ (Barnes, Kay, et al. 2016). The sample is then re-simulated using the zoom simulation technique to improve the resolution (Katz et al. 1993; Tormen et al. 1997; Barnes, Kay, et al. 2016). A dark-matter-only and hydrodynamic N-body simulation was run on the reduced zoomed volume. The high-resolution region of each zoom simulation extends to $5R_{200}$ of the cluster, where it is devoid of all low-resolution particles, such as those representing tidal forces of the cosmic web. R_{200} is described in equation 5.

E. Observational Theory

Cosmological simulations are often used to learn structure formation by cross-checking the observable properties of produced clusters at $z = 0$ to real-life ones, as MACSIS does successfully. However, these simulations also allow us to predict what to expect at greater redshift, so when observations are made it could provide useful to know what to look for. Or if what we observe is different to simulations, new cosmological models can be constructed.

For simulations, it is possible to determine M_{200} and R_{200} directly by summing the mass of particles within increasingly large radii, as described in section III. These are generally comprehended as the true mass and radius of the cluster and are represented in equation 5; however, the true mass is not an observable property of clusters. Rather, the mass of an observed cluster can be estimated by merging analytical models of X-ray density and temperature profiles under the assumption of hydrostatic equilibrium (F. A. Pearce et al. 2019).

1. X-ray

X-ray observations are a primary way to study clusters as little other cosmological objects produce X-rays. The high-temperature Intra-Cluster-Medium (ICM) ionizes the gas vacating lots of free high-energy electrons which radiate X-rays via Bremsstrahlung (free-free) emission (Sarazin 1986). The ICM is heated up by non-gravitational processes such as AGN feedback. Previous work, Cooper et al. (2022), investigated the change in baryon fraction using only hot X-ray emitting gas. The results concluded massive galaxy clusters consist of mostly hot gas, but groups consist of little-to-no hot gas. Most X-ray observations use R_{500} (an overdensity of 500 in equation 5) as within the gas is always in hydrostatic equilibrium (Evrard et al. 1996).

2. Sunyaev-Zeldovich Effect

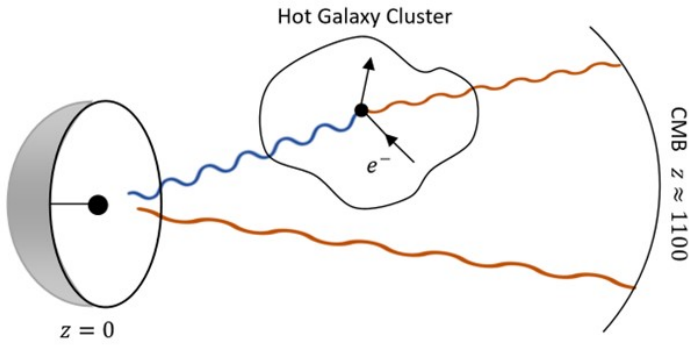


FIG. 2: Schematic of a CMB photon inverse Compton scattering off a high-energy electron in the ICM of a cluster. The blue line represents the blue-shifted Comptonised photon, and the red lines depict the CMB photons. The distortion is calculated by comparing the CMB photon directly and the scattered photon, figure 3. The left object represents a microwave detector at $z = 0$. The cluster's redshift is somewhere in between that and the CMB. Adapted image from Mroczkowski et al. (2019).

The Sunyaev-Zeldovich (SZ) effect provides an opportunity to probe galaxy clusters. This observation method relies on the fact that galaxy clusters are in the foreground of the Cosmic Microwave Background Radiation (CMB). The photons from the CMB pass through the cluster. The high-energy electrons in the hot X-ray emitting ICM of the cluster inverse Compton scatter these CMB photons (Carlstrom et al. 2002), see figure 2. This causes distortion to the very accurately known CMB spectrum in the line-of-sight of the cluster (Rephaeli 1995; Mo, C., et al. 2010; Fixsen 2009), see figure 3. The SZ effect, in principle, is independent of the redshift, making it the ideal observational tool for studying clusters at high redshift ($z \geq 1$). In this paper, we are only interested in the thermal SZ effect as just described. The kinetic SZ effect is an additional distortion due to the Doppler shift of the cluster's bulk velocity; however, this is negligible compared to the thermal SZ effect (Carlstrom et al. 2002). The thermal SZ effect distortion of the CMB expressed as an intensity change ΔI_V at dimensionless frequency $x = \frac{hv}{k_B T_{CMB}}$ is given by

$$\Delta I_V = y_{tSZ} I_0 \frac{x^4 e^x}{(e^x - 1)^2} \left\{ x \frac{e^x + 1}{e^x - 1} - 4 \right\}, \quad (6)$$

where I_0 is the CMB intensity:

$$I_0 = 2 \frac{(k_B T_{CMB}^3)}{(hc)^2}, \quad (7)$$

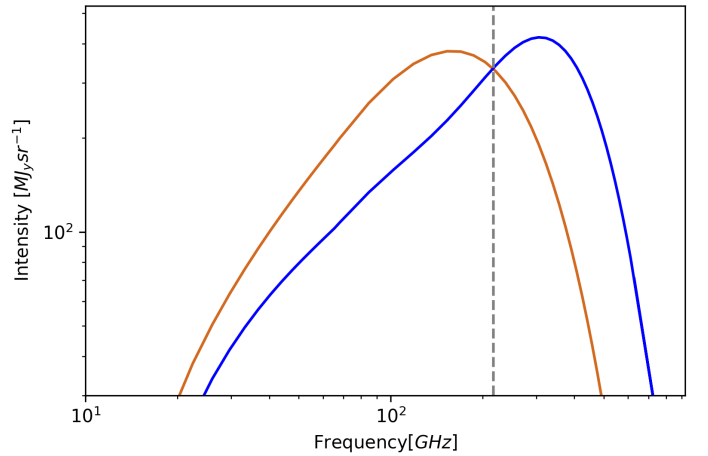


FIG. 3: The distortion (blue) of the CMB blackbody spectrum (red) using the first-order approximation SZ equation 6, as in Sunyaev and Zel'dovich (1980). As pointed out in Wright (2013), equation 6 is a bad approximation for a Compton y value of 0.15. However, real cluster data has y values in the order of 10^{-4} (figure 15), making the intensity plots almost indistinguishable. Nevertheless, $\Delta I_V / I_0$ is usually plotted, in which equation 6 becomes just as valid and even better for low y values than the exact approximation, (A8) in Sunyaev and Zel'dovich (1980). The grey dashed line indicates the frequency threshold of 217GHz, where below the SZ effect results in a decrease in the intensity of the CMB spectrum. This was plotted in matplotlib using data from the FIRAS instrument on the COBE satellite.

and h is Planck's constant, v is frequency in Hertz, k_B is Boltzmann's constant, T_{CMB} is the CMB temperature and y_{tSZ} is the thermal Compton- y parameter,

$$y_{tSZ} = \int \frac{k_B T_e}{m_e c^2} n_e \sigma_T dl = \frac{\sigma_T}{m_e c^2} \int P_e dl. \quad (8)$$

Here, T_e and m_e are the temperature and mass of the electron respectively, σ_T is the Thomson cross section, $P_e = n_e k_B T_e$ is the electron gas pressure and n_e is the electron density. The electron gas pressure is integrated over the line element dl along the line of sight. Therefore, the magnitude of the thermal SZ signal is an absolute measure of the integrated line of sight pressure (Mroczkowski et al. 2019; Carlstrom et al. 2002; Sunyaev and Zel'dovich 1980; Sunyaev and Zeldovich 1970).

The CMB photons have a low probability of interacting with high-energy electrons in the ICM ($\sim 1\%$). However, if they do interact, the inverse Compton scattering boosts the energy of the CMB photon by $\frac{k_B T_e}{m_e c^2}$ causing the distortion as shown in figure 3 (Carlstrom et al. 2002).

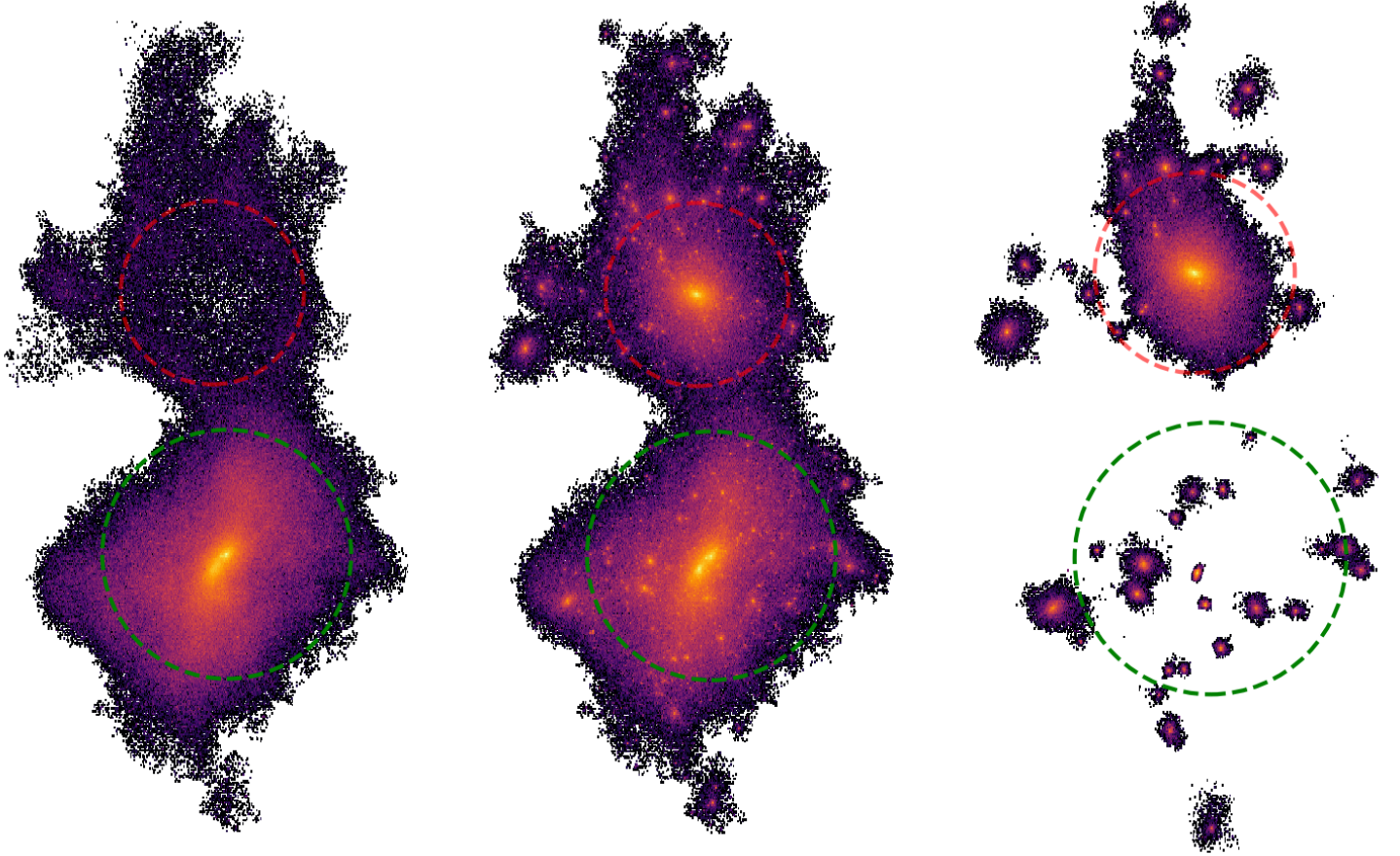


FIG. 4: An example of substructures found by SUBFIND, as thoroughly described in section III A. The aforementioned example is FoF halo 0 within the MACSIS halo 0, plotted using a mass-weighted heat map of only dark matter particles to exaggerate the substructure as gas particles are more diffuse. The left image only plots particles associated with *sub-group-number* = 0, representing the largest subhalo identified by SUBFIND, known as the background halo (Springel, White, et al. 2001). The middle image is a plot of everything in FoF halo 0, with no analysis by SUBFIND, used for reference. The right image plots particles identified with $1 \leq \text{sub-group-number} \leq 50$, representing the 50 largest substructures found by SUFIND. The dashed green ring is centred on the halo with the greatest centre of potential, with a radius of R_{200} of that background halo. The red-dashed ring highlights the largest subhalo found by SUBFIND, plotted with said halo's R_{200} . It has a M_{200} mass of $\sim 9.5 \times 10^{15}$, making it cluster based upon table I, and is situated $\sim 2.1R_{200}$ away from the background halo.

III. SUBSTRUCTURE

This section is standalone from the rest of the paper, going into further detail and analysing substructures (subhaloes) beyond the FOF algorithm discussed in section II D. Results outlined in other sections are solely based on structures found by FOF. This section is inspired by our previous work, Cooper et al. 2022, in which it was noticed that a halo had a large substructure that was not identified by the FOF algorithm, see figure 4. This section compares the properties of subhaloes and FoF haloes by plotting their baryon fraction (section III C) from an extended version of the FOF catalogue from our previous work to include subhaloes (section

III B) In summary, SUBFIND finds self-bound gravitational substructure (Natarajan et al. 2004; Springel, White, et al. 2001), see section III A for more detail.

Substructures in this paper are defined as all self-gravitating subhaaloes with lower mass than the centred background halo in each MACSIS zoom simulation. These subhaloes have a wide range of masses, and using our galaxy mass classification, table I, they range from sub-clusters to sub-groups. See figure 1 and figure 4 for an example of substructures found by the FOF algorithm and SUBFIND, respectively.

A. Identifying Substructures using SUBFIND

The most common technique to identify groups of virialized particles in cosmological simulations is the FoF algorithm, which links particles together closer than a set parameter, discussed in more detail in section II D. However, this method is problematic for finding substructures inside or in close proximity to larger virialized structures because these independent substructures become linked. Furthermore, two independent structures could be linked by small particle bridges (Springel, White, et al. 2001). A consequence of both of these shortcomings leads to independent substructures becoming unidentified, such as the large structure in figure 4, which is missing data.

Every MACSIS hydrodynamic N-body zoom simulation was post-processed with SUBFIND to identify substructures in the FoF haloes. Within a FoF halo, every particle's density is estimated with an adaptive kernel interpolation method using a standard SPH approach. This results in a density field that consist of locally overdense regions, each identified as a substructure candidate. The edge of every substructure candidate is resolved by reaching a saddle point in the density field before getting to the level of the background halo. Finally, every candidate undergoes a gravitational unbinding procedure where all unbound particles are removed. The substructure is recorded as an authentic subhalo if it has more bound particles than a set minimum threshold (Springel, White, et al. 2001; Dolag et al. 2009). Particles belonging to specific FoF haloes and their underlying subhaloes can be highlighted in MACSIS using *group-number* and *sub-group-number*, respectively. *sub-group-number* = 0 separates the main background halo from all other subhaloes in their respective FoF halo. Moreover, *sub-group-number* ≥ 1 designates the subhaloes in descending mass order.

Unfortunately, unlike the FOF algorithm, SUBFIND does not calculate M_{200} and R_{200} values and only provides the total mass of bound particles. The method of manually calculating these values began with ranking all particles in ascending order of distance from the substructure's centre of potential. The particle order was ascended, and the density was calculated, using the mass as the sum of all particles below that particle in the list and the radius as the distance to that particle. When the density equals 200 times the critical density (ρ_{cr}), the mass and radius equate to M_{200} and R_{200} as defined in equation 5. See appendix A for more detail. Comparing known FoF haloes with background haloes from SUBFIND, this method accurately calculates M_{200} and R_{200} to within two decimal places. The subhaloes must pass some selection criteria to be appended to the catalogue.

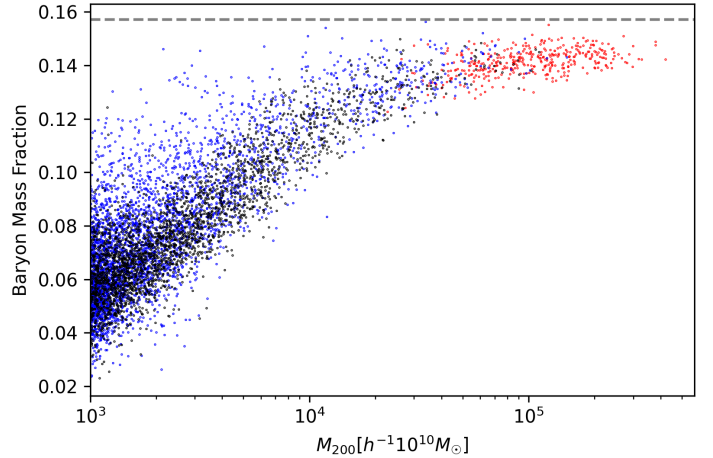


FIG. 5: Baryon fraction against halo M_{200} plot from previous work at $z = 0$, Cooper et al. (2022), overlayed with blue subhalo data points. The red and black points are the main progenitors and smaller haloes of FoF haloes, respectively. The dashed grey line represents the universal baryon fraction $f_b = \Omega_b/\Omega_m = 0.157$.

B. Catalogue Extension

The selection criteria placed on the subhaloes are as follows; $M_{200} \geq 10^{13}$ to represent a group, must be devoid of low-resolution particles within R_{200} , and must not be within R_{200} of any other halo as this overlap would have negatively impacted the M_{200} and R_{200} calculations. All valid subhaloes are now added to the preliminary catalogue.

Previous work, Cooper et al. (2022), produced a candidate catalogue of FoF haloes for every redshift using the same first two selection criteria. This catalogue is now extended to include the valid subhaloes found within every FoF halo. For context at $z = 0$, 3547 valid subhaloes are added to the catalogue. This more than doubles the original catalogue of 3085 FoF haloes, which shows how much substructure is missing by using the FoF algorithm standalone. However, the number of subhaloes as a fraction of FoF haloes decreases with increasing redshift suggesting substructures are more independent and refined at greater redshift.

The data stored regarding every halo in the catalogue is; MACSIS halo, FoF halo, *sub-group-number*, M_{200} , x, y, z coordinates, R_{200} , total bound mass, and their baryon fraction. Seven total catalogues exist for the different snapshots taken by MACSIS. Snapshots are taken at various redshift intervals, in which all current particle data is recorded and can be retrieved via snapshot files. In this project, the snapshots used represent $0 \leq z \leq 3$.

C. Substructure Baryon Fraction

The baryon fraction is calculated by dividing the summed mass (M_x) of all baryonic particles by the total summed mass within R_{200} of the centre of a halo,

$$f_b = \frac{M_{\text{gas}} + M_{\text{stars}}}{M_{\text{gas}} + M_{\text{stars}} + M_{\text{darkmatter}}} = \frac{M_{\text{gas}} + M_{\text{stars}}}{M_{200}}, \quad (9)$$

Their baryon fraction was plotted against M_{200} as shown in figure 5 to compare these subhaloes with FoF haloes. Most of the subhaloes follow the prior trend of increasing baryon fraction with mass. This is because higher mass haloes have greater gravitational potential wells that retain baryon content being ejected from feedback processes more efficiently, discussed in more detail here [Cooper et al. \(2022\)](#). However, some subhaloes deviate from this trend by over-calculating their baryon fraction, specifically at $M_{200} \leq 10^{14}$. This could be due to some overlapping of substructure SUBFIND could not resolve.

IV. RADIAL PROFILES

This section investigates the hot gas density (ρ_{gas}), thermal pressure (P_{th}) and temperature (T) radial profiles of three distinct mass bins representing groups, clusters and massive clusters (table I) to search for self-similar evolution. The effect cluster merges have on the self-similar evolution of the ICM is also conducted via a case study. If the radial profiles of two haloes are similar, it can be said they exhibit self-similar behaviour. Henceforth, the three mass bins will be referred to as group bin, cluster bin and massive clusters bin. Under the simplest model, dark matter halo formation occurs due to the gravitational collapse of overdense regions in the dark matter distribution. The baryons are heated to the virial temperature by gravitational processes such as adiabatic compression and shock heating during the collapse; see section II B and [Cooper et al. \(2022\)](#) for more detail on all processes. Because only non-linear processes occur, clusters are expected to be scaled versions of each other, known as self-similar. Additionally, assuming clusters are spherically symmetric, the ICM can be said to be in hydrostatic equilibrium with the dark matter potential well, allowing us to derive self-similar scaling relations between cluster properties using $E(z)$ (equation 4) ([Short et al. 2010](#); [Maughan et al. 2012](#); [Kaiser 1986](#)).

All calculations use **hot gas** ($\geq 10^6 K$) **particles** to represent the hot X-ray emitting ICM. This is done to simulate

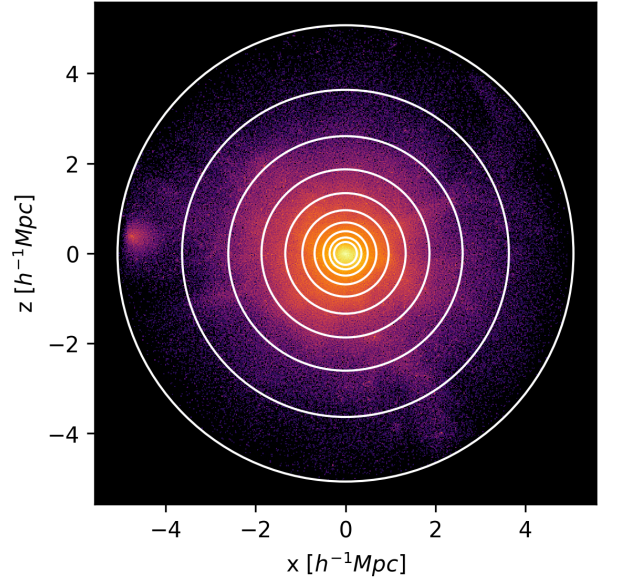


FIG. 6: A logged hot gas 2D distribution of FoF halo 0 at $z = 0$ with ten logarithmically spaced bins, $(0.1-2)R_{200}$, superimposed on top. The volume of each shell, V_{shell} , is calculated using $V_{\text{shell}} = \frac{4}{3}\pi(r_2^3 - r_1^3)$. Here, r_2 is the outer radius, and r_1 is the inner radius of a shell. x and y are comoving coordinates.

X-ray and SZ observations, as discussed in section II E. Furthermore, from previous work [Cooper et al. \(2022\)](#), it was found MACSIS massive clusters are mostly hot gas regardless. All radial profiles are normalised using their virial counterparts, presented in sections IV A, IV C, IV B respectively, to remove the self-similar mass and redshift dependence extrapolated from gravitational heating.

- Halo data used is from previous work's candidate catalogue, [Cooper et al. \(2022\)](#) section III, and is discussed in section III B and I. In summary, all haloes utilised are derived from the FoF algorithm, with a lower mass limit of 10^{13} and are devoid of low-resolution particles. The redshift evolution is taken over $z = 0.0, 0.46, 1.0, 1.56, 2.05, 2.69, 3.0$.

A radial profile represents a distribution of matter as a function of distance from the centre of a halo. For a three-dimensional object, such as a halo, the distribution of matter is modelled in 3D concentric shell bins around the centre of potential. This paper uses ten logarithmically spaced bins from $0.1 \leq R_{200} \leq 2$ around every FoF halo, as shown in figure 6. The volume of each shell is denoted as V_{shell} .

The bins are logarithmically spaced because when the radial profiles are plotted with logged axes, the profile gradient depends on mass, which is used in hydrostatic equilibrium to

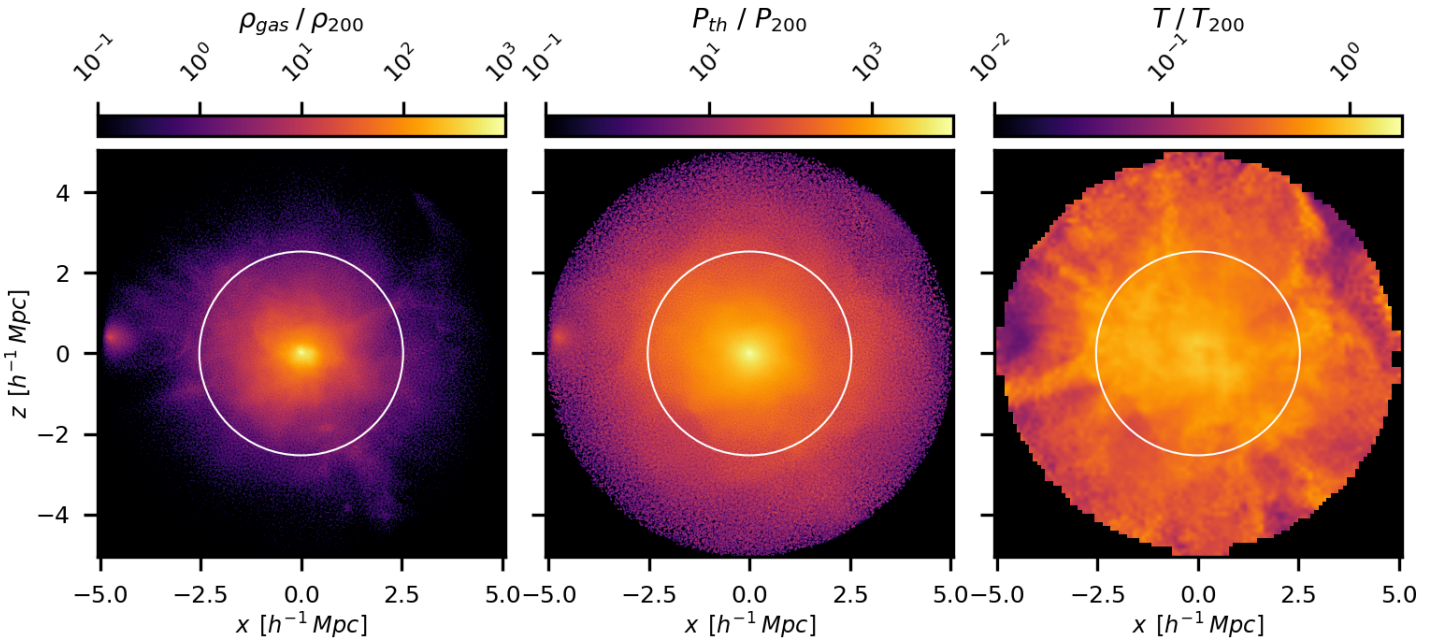


FIG. 7: Projected hot gas maps plots within $2R_{200}$ of FoF halo 0 over 500^2 bins. The left plot is mass-weighted, representing the hot gas's density distribution, and is consequently normalised to the virial density ρ_{200} , equation 10. The thermal pressure is conveyed via the middle plot, which is mass-temperature-weighted, and hence normalised to the virial pressure P_{200} , equation 16. The right plot represents the temperature distribution by using mass-weighted temperature and is normalised to the virial temperature T_{200} , equation 13. The white ring shows the position of $1R_{200}$. All plots are logged to enhance their visual properties. The main visual difference is how diffuse they are; the density plot falls off just after R_{200} , whereas the pressure and, even more so, the temperature plots appear to be more diffuse across $2R_{200}$. All maps are smoothed using a Gaussian interpolation.

estimate the halo's mass. The cluster's core ($\leq 0.1R_{200}$) is not included because it is messy and includes unsimulated physics, such as thermal conduction, which impacts feedback efficiency from black holes (Barnes, Kannan, et al. 2019). The radial profiles extend out to $2R_{200}$ to test for self-similarity at larger radii outside the virial radius.

The median profiles are computed at each redshift interval by calculating the individual radial profile for every FoF halo in the catalogue. The logarithmic bins are placed on every halo, and the profile is calculated, yielding ten values for each bin. However, since the value calculated is an average across that bin, each value is assigned the radius at the centre of the bin ($0.12 \leq R/R_{200} \leq 1.7$), not the edge radius. Now that we have radial profiles for every FoF halo at ten radius intervals, they are grouped into the three mass bins (table 1), and then the median at each radius is taken to produce one overall profile for each mass bin at every redshift. A minimum bin size of 10 is required to get plotted to reduce the influence of any outliers. The minimum radii averaged over is the core radius ($r_c \simeq 0.12R_{200}$).

A. Density Profile

Density profiles of dark matter haloes provide information about how matter is distributed on small scales at the core of haloes, relating to the non-gravitational processes that occur, and on the large scales with clusters where gravitational processes dominate. Additionally, they can be used to estimate a dark matter haloes total mass under the hydrostatic equilibrium assumption.

Figure 7 visually shows a dark matter halo's hot gas mass distribution. As expected, the densest region of hot gas is in the centre where gravitational heating, such as adiabatic compression, and non-gravitational heating, such as AGN feedback, have the strongest influence. The distribution quickly falls off outside the virial radius R_{200} .

The density radial profile is calculated using the concentric shells and their volume V_{shell} , illustrated in figure 6. The density is integrated across the radius of a shell. However, as we have access to every particle inside every shell, we can

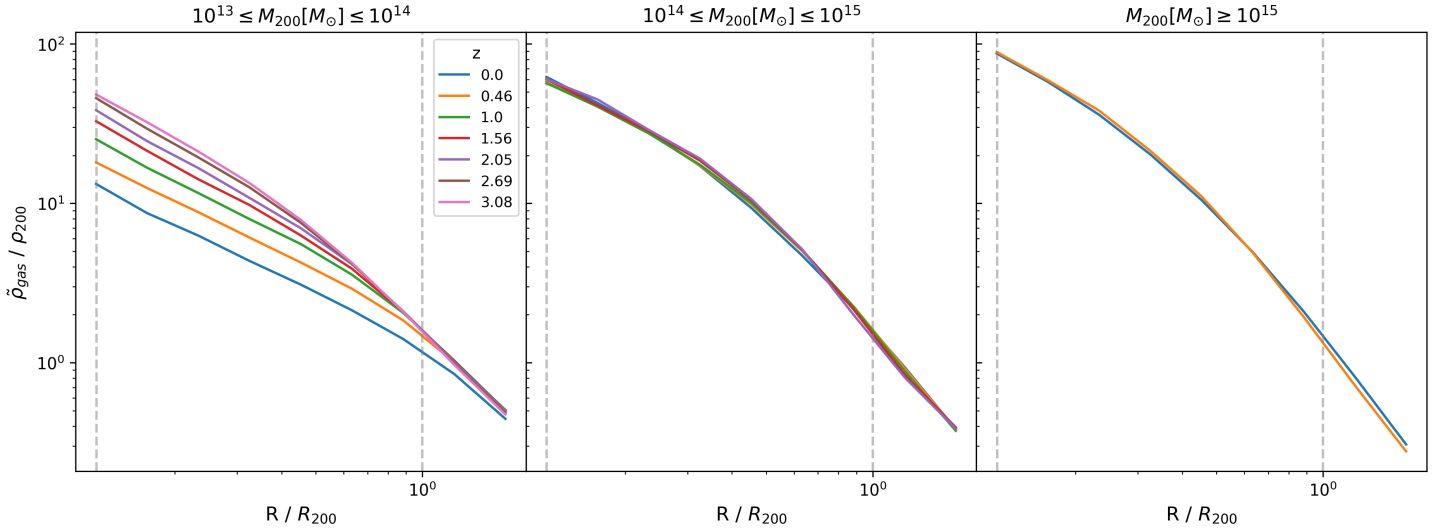


FIG. 8: Normalised median hot gas density versus normalised radius of each bin (group bin on the left and massive cluster bin on the right, shown at the top of the figure) for $z = 0.0, 0.46, 1.0, 1.56, 2.05, 2.69, 3.0$ as displayed by the legend in the left plot. The middle plot indicates that clusters do not exist beyond $z \geq 2.05$. Similarly, the right plot reveals massive clusters have not formed until $z = 0.46$. The left grey dashed line on each subplot represents the core radius (r_c) and the right dashed line is placed at the virial radius (R_{200}).

calculate the radial density discretely,

$$\rho_{gas}(r) = \frac{1}{V_{shell}} \int_{V_{shell}} \rho(r) dr = \frac{1}{V_{shell}} \sum_i^{N_{shell}} m_i, \quad (10)$$

where N_{shell} is the total number of particles in each shell, and m is the mass of an individual particle. This is normalised to the virial density,

$$\rho_{200} = \frac{\Omega_b}{\Omega_m} \rho_{cr,co} \Delta_c. \quad (11)$$

Here, $\Omega_b/\Omega_m = \bar{f}_b = 0.157$ as demonstrated in figure 5, $\rho_{cr,co}$ is the comoving critical density (equation 3 multiplied by equation 1), and the overdensity $\Delta_{cr} = 200$ (equation 5).

The redshift evolution of normalised median hot gas density profiles is plotted for each mass bin in figure 8. For groups, the density is spread out in ascending redshift order from bottom to top at lower radii. This is due to a similar problem with groups discussed in section III C. At lower redshifts, when group cores are denser, the feedback processes become more violent and the shock radius fraction (R_S/R_{200}) increases (Lau et al. 2015). This feedback, such as shock accretion, blows out the gas and heats it more easily; the lower gravitational potential wells of groups are not as efficient at retaining baryons resulting in a drop in gas density. However, at $\sim R_{200}$, most of the redshift profiles converge to evolve self-similarly, with the $z = 0$ profile joining at larger radii. Here, the influence of feedback processes

becomes negligible compared to gravitational physics to the ICM density outside the virial radius.

In contrast to the group bin, clusters and massive clusters are remarkably self-similar across the entire radius range for all redshifts. There is no redshift evolution of clusters or massive clusters over the probed redshift and radius range. The hot gas, and hence the ICM, density profiles are fully consistent with expectations from the self-similar model, $\propto E(z)^2$. A closer look at the core radius in figure 9 shows the steady decrease of density spread across redshifts for more massive dark haloes. Yet, The mean core density increases simultaneously. This can be accredited to larger gravitational wells causing more ICM to fall into the centre that adiabatically compresses, making it denser at the core radius.

Our ICM density results closely match density profiles created via X-ray observations. However, most X-ray observations focus on clusters and larger and not groups because they are generally more of interest and contain more X-ray-emitting hot gas. Furthermore, as briefly discussed in section II E 1, it is popular for X-ray observations that intend on estimating the total dark matter halo mass via the hydrostatic equilibrium assumption to use R_{500} because it ensures that the hot gas enclosed by this smaller radius is in hydrostatic equilibrium. Hence, makes the assumption more valid and should yield more accurate results. However, as we do our analysis in terms of the virial radius R_{200} it can become increasingly difficult to compare results exactly. Nevertheless,

[Maughan et al. \(2012\)](#) look at both groups and clusters from $0.1 \leq z \leq 1.2$, which replicate the density redshift spread at lower radii using a collaboration of X-ray observations. A simulation, namely *Omega500* from [Lau et al. \(2015\)](#), plotted the normalised density profile for lower mass clusters in the range $0 \leq z \leq 1.5$. They found normalising with the $200 \times \rho_{cr}$, as we do, the inner regions appear more self-similar, whilst the outskirts of the cluster are more self-similar when normalised with respect to the mean density of the universe. Observational comparisons include [A. Vikhlinin et al. \(2006\)](#) and [McDonald, Allen, et al. \(2017\)](#) for $0 \leq z \leq 1.9$. One difference between these MACSIS-simulated ICM profiles and X-ray observation profiles is that they depart from observations below the core radius. [McDonald, Allen, et al. \(2017\)](#) directly compared ICM density profiles of X-ray observations to MACSIS and found that simulated cluster cores are too dense in comparison. It is considered that the included physics in MACSIS is insufficient to replicate the interplay between the AGN and the ICM. However, it can be concluded that outside the core radius, MACSIS simulations yield an ICM density that matches X-ray observations and is self-similar. Considering this, as our density profiles extend to $z = 3$, they should be a good approximation to what would be observed for protoclusters.

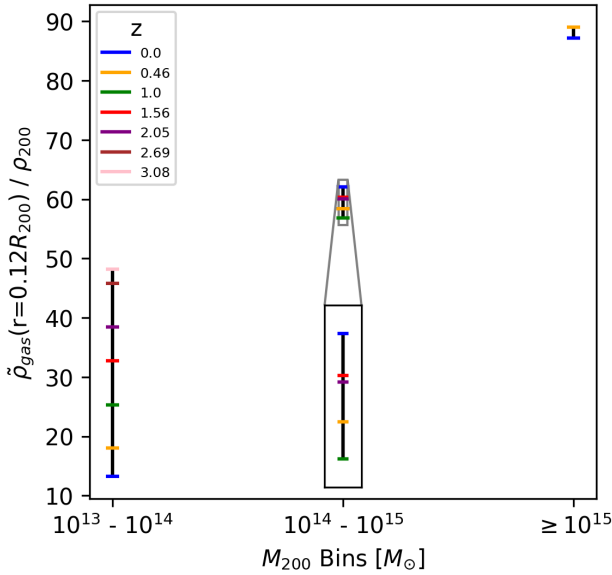


FIG. 9: Normalised median hot gas density at the critical radius ($r_c = 0.12R_{200}$) for the three mass bins of dark matter haloes. The density's redshift evolution at the core radius decreases as the dark matter halo increases in mass. Moreover, the mean density also increases for larger mass bins. The cluster mass bin is zoomed in to clarify the number and order of redshifts. The left grey dashed line in figure 8 illustrates the radius at which this figure is plotted.

B. Temperature Profile

Temperature profiles of dark matter haloes are useful for a few reasons. As dark matter does not interact with electromagnetic radiation, the temperature profile can aid the understanding of the dark matter distribution. Moreover, temperature profiles can be used alongside the density profile to estimate the cluster's total mass under hydrostatic equilibrium and to study the baryonic and feedback processes that occur in the core of a cluster by observing its temperature influence on the ICM. The normalised projected temperature distribution of a dark matter halo can be seen in figure 7. As we are only using gas particles with a high-temperature threshold of $T \geq 10^6 K$ there lacks depth to the distribution when normalised.

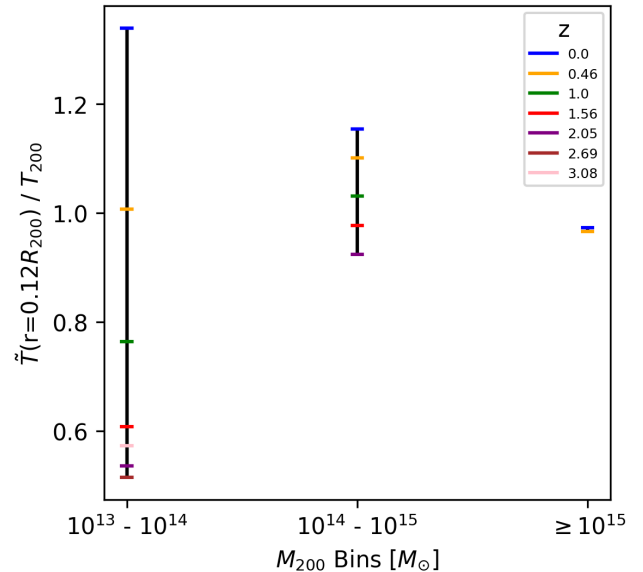


FIG. 10: Normalised median temperature at the critical radius ($r_c = 0.12R_{200}$) for the three mass bins of dark matter haloes. Comparable in trend to figure 8, the core radius temperature's redshift evolution decreases as the dark matter halo increases in mass. However, the mean temperature remains roughly constant across the mass bins.

The temperature radial profiles are computed in each concentric bin using,

$$T(r) = \frac{\sum_i^{N_{shell}} m_i T_i}{\sum_i^{N_{shell}} m_i}, \quad (12)$$

where T_i is the temperature of individual particles in the bin. The temperature is normalised to,

$$T_{200} = \frac{GM_{200}}{2R_{200}} \left(\frac{\mu m_p}{k_B} \right). \quad (13)$$

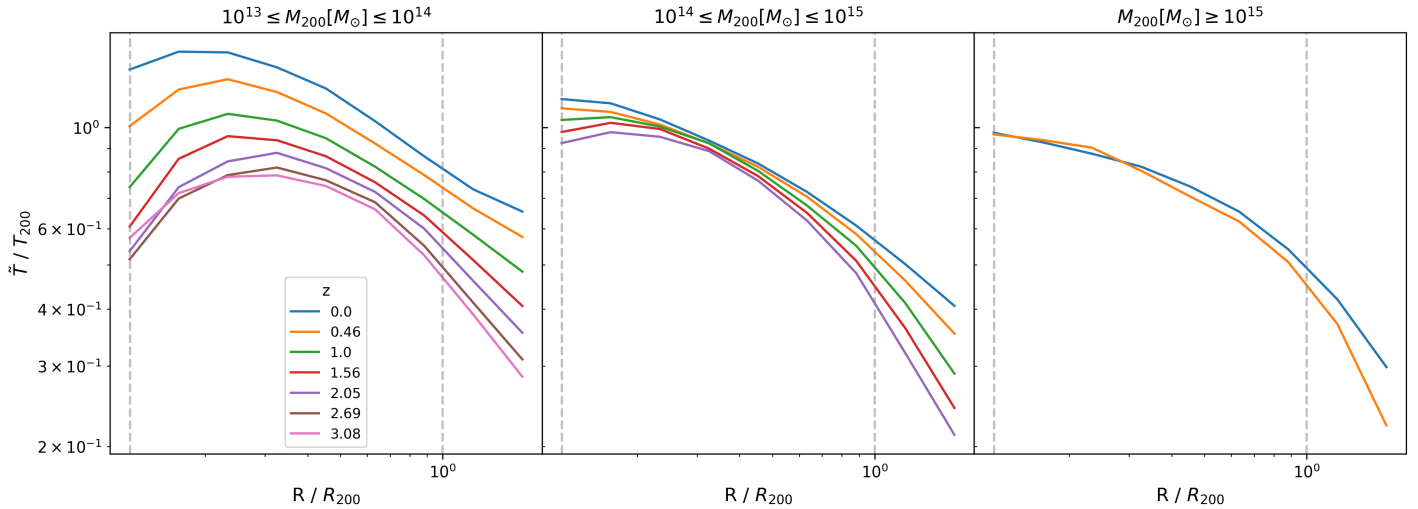


FIG. 11: Normalised temperature versus normalised radius of each bin following the same layout, linestyle and redshift colour scheme as figure 9. Additionally, it also suggests that clusters and massive clusters have not formed until $z = 2.05$ and $z = 0.46$, respectively.

Here, $\mu = 0.59$ is the mean molecular weight assuming a fully ionized plasma, m_p is the mass of a proton assuming the ICM is just hydrogen, and M_{200} and R_{200} are the virial parameters described in equation 5.

Figure 11 shows the median normalised temperature profiles in the same layout as figure 8. All mass bins have distinct profile shapes in redshift spread and curvature. The group bin temperature redshift profiles peak between $0.1 - 0.3R_{200}$, the cluster's profiles flatten as they reach the core radius, and the massive cluster's mass-weighted temperature continues to increase into the core. The temperature profile peak is consistently at larger radii for higher redshift dark matter haloes. These peaks can be seen in low z observations A. Vikhlinin et al. (2006), with radiative cooling being responsible. The peak is premature in the group bin specifically due to a similar philosophy discussed in section IV A. The lower gravitational potential wells of groups allow feedback processes to blow out gas particles more efficiently. Further, the denser environments at the centre allow stars to form using gas particles. Evidence for this was divulged when calculating the temperature profiles using equation 12 at lower radii; it would occasionally return `numpy.nan` because there were no hot gas particles to sum inside the bin.

The core radius normalised median temperature profiles are shown in figure 10. The mean temperature remains roughly constant across the mass bins due to the groups' and clusters' decreasing and flattening profiles, respectively. The redshift evolution of temperature profiles is also present; for every bin and at every radius, the normalised temperature decreases with increasing redshift, observed in McDonald,

Benson, et al. (2014). This is because high z dark matter haloes have a higher physical mass accretion rate. Therefore, their accretion shocks can penetrate further by driving the low-temperature pre-shock regions towards the core radius (Lau et al. 2015). As the temperature drops, the density increases due to hydrostatic equilibrium.

Within groups, there is very little evidence for self-similar evolution. Clusters only become self-similar in a narrow region, $0.2 \leq R/R_{200} \leq 0.4$. However, massive clusters exhibit self-similarity at small radii, with the profiles slowly departing as the radius increases, matching the other two bins.

At $z = 0$, normalised medium temperature profiles align with other simulations such as F. A. Pearce et al. (2019) and somewhat align with cluster X-ray observations in A. Vikhlinin et al. (2006). Another older X-ray observation De Grandi et al. (2002) for clusters and massive clusters agree with our profile plots much better at $z = 0$. Different simulations have created other spectroscopic-like (X-ray) temperature profiles over a range of redshifts. The *Millennium Gas PC run* produces a similar shape to our massive cluster normalised temperature profiles, but the redshift evolution is reversed to $z = 1.5$. The temperature profiles increase with redshift; they have accredited this to compression and shock heating occurring at a lesser rate in the self-similar gravitational heating model. However, a simulation released similar to MACSIS called *Omega500* produced median temperature profiles with the same redshift evolution out to $z = 1.5$, by Lau et al. (2015). Their cluster profiles extend to larger radii, enhancing the spread we started to see in figure 12. They experience self-similarity for clusters across similar regions.

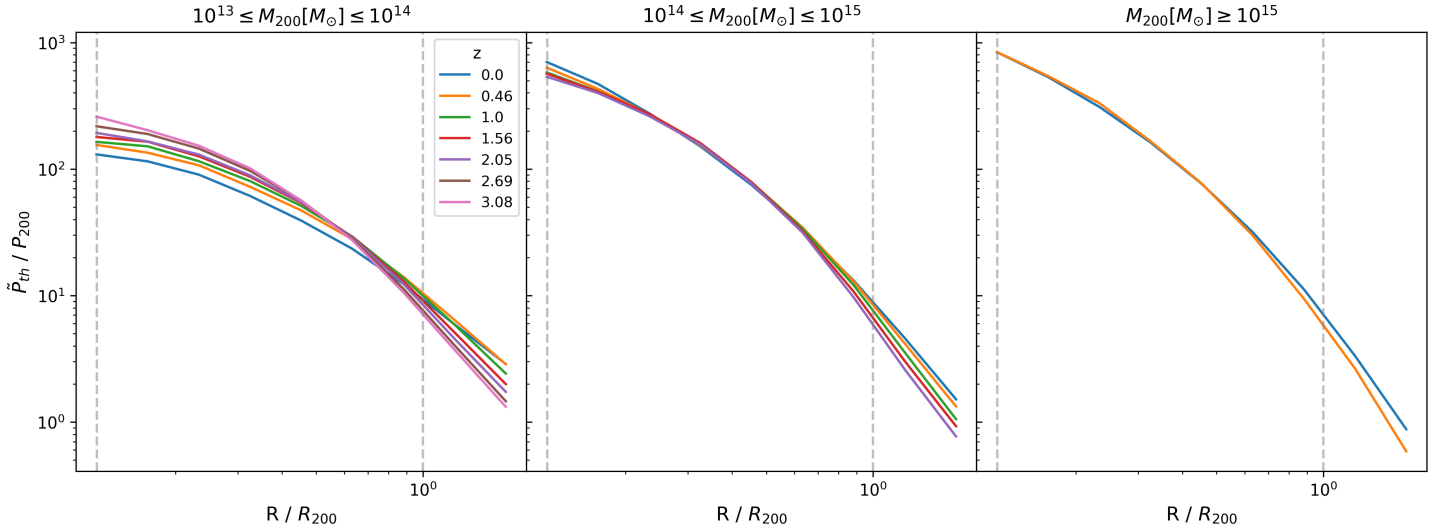


FIG. 12: Normalised median thermal pressure versus normalised radius of each bin following the same layout, linestyle and redshift colour scheme as figure 8. Additionally, it also suggests that clusters and massive clusters have not formed until $z \geq 2.05$ and $z = 0.46$, respectively.

C. Thermal Pressure Profile

Thermal pressure is created by the infall of baryonic gas into the centre of the potential of the dark matter halo, where it is adiabatically compressed and shock heated to $T \geq 10^6 K$. This thermal pressure is the primary outward force balancing the gravity of the enormous dark matter haloes, stopping the halo from collapsing. This makes the thermal pressure a key property of a dark matter halo and is observed via X-ray emission or scattered CMB photons from the SZ effect, where the theory is discussed in section II E 2 and replicated in section V. For this section, we are just interested in the X-ray emission. Figure 7 shows the thermal pressure distribution of the ICM in a dark matter halo. It appears to be more diffuse across $2R_{200}$ than the density distribution. This is in contrast with comparing figures 8 and 12 as pressure profiles are steeper, however, this could be because the profiles are a median value.

The hot gas (thermal) pressure profiles were calculated by combining the temperature and density profiles,

$$P(r) = \rho(r)T(r)\frac{k_B}{\mu m_p}, \quad (14)$$

which yields,

$$P_{th}(r) = \frac{k_B}{\mu m_p V_{shell}} \sum_i^{N_{shell}} m_i T_i. \quad (15)$$

This is used to compute the pressure profile for each concentric bin. It is then normalised to the virial pressure,

$$P_{200} = \frac{\rho_{cr,co} k_B T_{200}}{\mu m_p}, \quad (16)$$

where, $\rho_{cr,co}$ is the comoving critical density, and T_{200} is the virial temperature from equation 13.

Figure 12 plots the redshift evolution of the normalised median thermal pressure across the three mass bins. The group bin lacks evidence of self-similarity, but interestingly there is a redshift profile cross-over at around $0.7 - 0.8 R_{200}$. The order flips from increasing thermal pressure with increasing redshift at the core to decreasing thermal pressure with increasing redshift outside the virial radius. Outside the virial radius, the group redshift evolution of the profile matches that of the clusters and massive clusters. Therefore, this cross-over point might represent where the gravitational processes take over the baryonic and feedback processes in low-mass dark matter haloes such as groups. The cluster and massive cluster bins loosely resemble the temperature profiles in figure 11, with tighter redshift spreads. This would make sense because the pressure combines the temperature with the strong self-similar density profiles. The cluster bin profiles collapse to a single profile for $0.2 \leq R/R_{200} \leq 0.7$ and retain the same redshift order at the core and outside R_{200} . The massive cluster bin retains self-similarity for the entire range. The redshift evolution of the median pressure profiles is due to the combination of the processes discussed in sections IV A and IV B.

Figure 12 shows the average core thermal pressure increase with increasing mass; this matches X-ray observations such

as Arnaud et al. (2010). The thermal pressure increases for more massive dark haloes because it has to balance the larger gravitational pressure to stop the halo from collapsing.

X-ray observations such as Planelles, Fabjan, et al. (2017), in agreement with other observations McDonald, Benson, et al. (2014) and simulations Battaglia et al. (2012), provide scaled thermal pressure profiles of clusters and groups that show little evidence for redshift evolution for $0.5 \leq z \leq 0.8$. They state the lack of evolution suggests that any non-gravitational processes must have occurred at earlier epochs. However, even at these redshifts, we observe some significant evolution in clusters at the core radius and outside the virial radius. In McDonald, Benson, et al. (2014), a larger z range is covered $0 \leq z \leq 1, 2$, and we replicate the increase of the core pressure for lower z in clusters but not to the same extreme extent in figure 13. This is boosted by the increase of temperature at lower redshifts seen in figure 11. Yet, the simulation in Lau et al. (2015) again agrees with our results by exhibiting the same redshift evolution at the core radius and at larger radii.

There seems to be some agreement and disagreement with other studies on the redshift evolution of thermal pressure profiles. However, the next section covers a different observation method that also uses the thermal pressure known as the SZ effect, which is independent of redshift in principle.

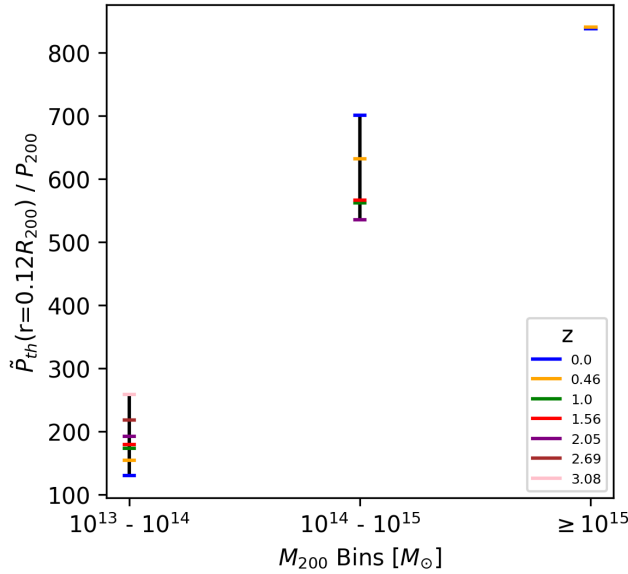


FIG. 13: Normalised median thermal pressure at the critical radius ($r_c = 0.12R_{200}$) for the three mass bins of dark matter haloes. Unlike the trend in figure 9, the redshift spread of the core pressure is consistent for groups and clusters and then decreases for massive clusters. However, the mean core pressure still increases for more massive dark matter haloes.

D. Merging Clusters

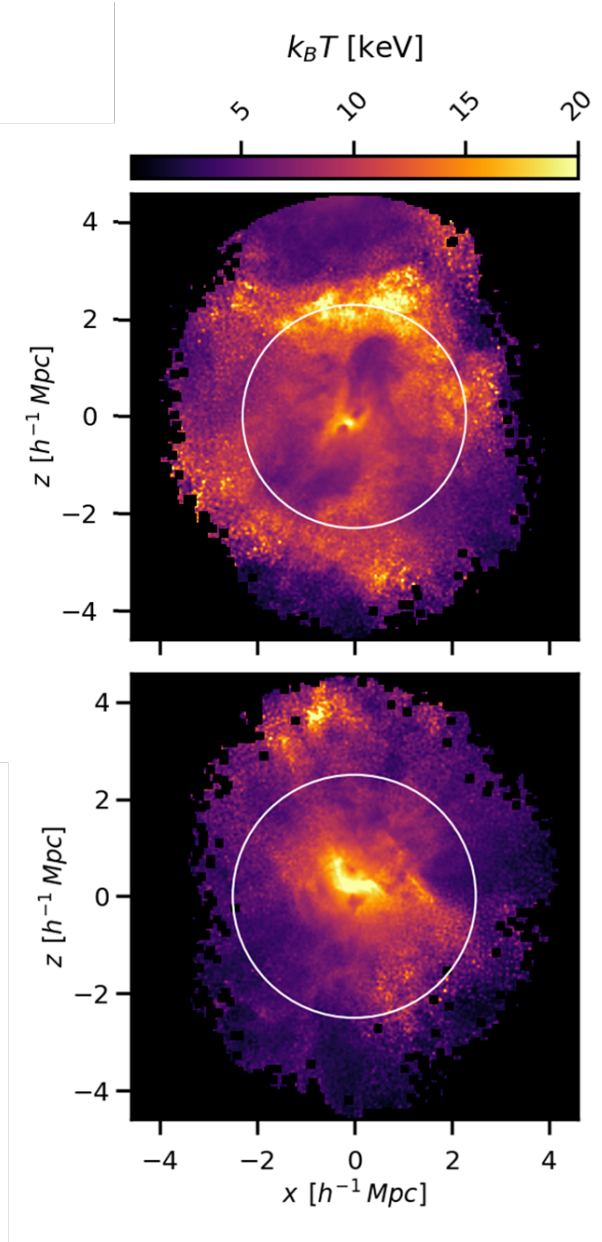


FIG. 14: Projected temperature distribution using mass-weighted temperature for MACSIS halo 1 with a field of view of $2R_{200}$. The top plot is at $z = 0$ at the beginning of the merger. The bottom plot is at $z = 0.14$ before the merger has any effect; the incoming structure can be seen directly above the central halo. These are plotted similarly to 7, but instead of normalizing to the virial temperature, it is scaled to $k_B T$ in keV. This allows for a great amount of depth to be seen, and the temperature of sections of the distribution can be directly inferred.

This section covers merging clusters and their effect on the ICM and self-similar evolution. Under Λ CDM cosmology,

the formation of clusters relies on the constant merging of structure. Collisions between massive clusters are some of the most energetic events at this current epoch. The projected temperature profile distribution for a merging massive cluster and cluster is shown in figure 14. This is the same halo used to discuss substructures in section III, and the dark matter structure is shown in figure 4. These two structures were linked with the FoF algorithm.

Whilst the mergers occur due to gravitational attraction, the effect on the ICM can be very hydrodynamical. The ICM is heated through supersonic shocks caused by kinetic energy dissipation (Bourdin et al. 2013). Figure 14, shows the early stage of a two-cluster merger. Two shocks front are created when the boundaries of the two clusters collide. These shock fronts carry high entropy gas away whilst propagating in the cluster, forming two cold fronts. The cold fronts propagate the clusters but cannot penetrate, leaving a banded shock front of high-temperature gas between the merging clusters (Bourdin et al. 2013). A similar description for the temperature redshift evolution was described in section IV B (Lau et al. 2015). This shock front can be seen in the top image of figure 14 is roughly twice as hot as the temperature inside the virial radius.

A paper, Moura et al. (2020), simulates the merging of the *Abell 2034* cluster. They simulate the shock front between two merging clusters for objects with mass $M_{200} = 2.35 \times 10^{14} M_\odot$ and $M_{200} = 1.08 \times 10^{14} M_\odot$. Therefore, the peak temperature observed in the shock front is less than our MACSIS one at 12keV. However, similar peak temperatures are achieved if we scale the mass with ours.

Mergers affect the self-similar evolution because the temperature profile gradient of merging clusters is drastically different than the median profile. This is obviously because the hot shockfront disrupts the natural decrease of temperature with increasing radii. The effect merging has on the SZ Compton- y value is discussed in Motl et al. (2005).

V. THERMAL SUNYAEV-ZELODOVICH CLUSTER MAPS

This section develops the projected X-ray thermal pressure maps created in section IV, see figure 7, to create thermal SZ maps. The underlying theory behind the SZ effect is described in detail in section II E 2. In summary, the thermal SZ effect provides an opportunity to study the ICM via CMB photons that have inverse Compton scattered off free high-energy electrons. The ICM boosts the energy of a CMB photon which can be observed via a fluctuation in the inten-

sity of the CMB spectrum. Since the SZ effect is based on scattering, its magnitude is independent of redshift, making it ideal for high redshift dark matter haloes such as protoclusters.

Equation 8 showed that the magnitude of the thermal SZ signal was an explicit measurement of the integrated thermal electron pressure in the line of sight. By substituting in equation 14, we assume that in the ionized ICM the thermal electron pressure can be approximated to the thermal gas pressure, $P_e \approx P_{th}$,

$$y_{tSZ} = \frac{\sigma_T}{m_e c^2} \int \rho(r) T(r) \frac{k_B}{\mu_e m_p} dl, \quad (17)$$

where $\mu_e = 1.14$ is the mean molecular weight of an electron and c is the speed of light. The pressure along the line of sight is integrated by evaluating y_{tSZ} in a single projected pressure map pixel by discretising the y_{tSZ} integral to a cube of volume V . If the cube has a pixel area A_{pix} along the line of sight we can use $dV = A_{pix} dl$ and substitute it into the equation above,

$$y_{tSZ} = \frac{\sigma_T k_B}{\mu_e m_p m_e c^2 A_{pix}} \int \rho(r) T(r) dV. \quad (18)$$

Much like the radial thermal pressure in equation 15 the integral can be represented in the discrete version,

$$y_{tSZ} = \frac{\sigma_T k_B}{\mu_e m_p m_e c^2 A_{pix}} \sum_i^{N_{gas}} m_i T_i, \quad (19)$$

which expresses the mass-weighted temperature of hot gas particles summed over the projected pixel volume. This derivation follows Silva et al. (2000). Figure 7 uses 500 bins, yielding total number of pixels $N_{pix} = 500^2$. The A_{pix} is converted to a length in Mpc by dividing the width or height of the plot by the number of pixels in that direction.

Figure 15 shows the computed thermal SZ effect, using equation 19, of a massive MACSIS cluster from $(0 - 3.08)z$. The cluster has a virial mass $M_{200} \sim 3.7 \times 10^{15} [h^{-1} M_\odot]$. By using equation 19 we expect y_{tSZ} to increase with cluster mass and temperature. We observe a steady increase from $z = 3.08$ to $z = 0.46$, but at $z = 0$ it sharply decreases. However, the average y_{tSZ} value for the cluster is still in the order of magnitude of 10^{-4} , which agrees with what is discussed in figure 3 and other simulations Kay et al. (2012). The y_{tSZ} distribution is very smooth, also comparable to other simulations Kay et al. (2012) and Motl et al. (2005) at $z = 0$.

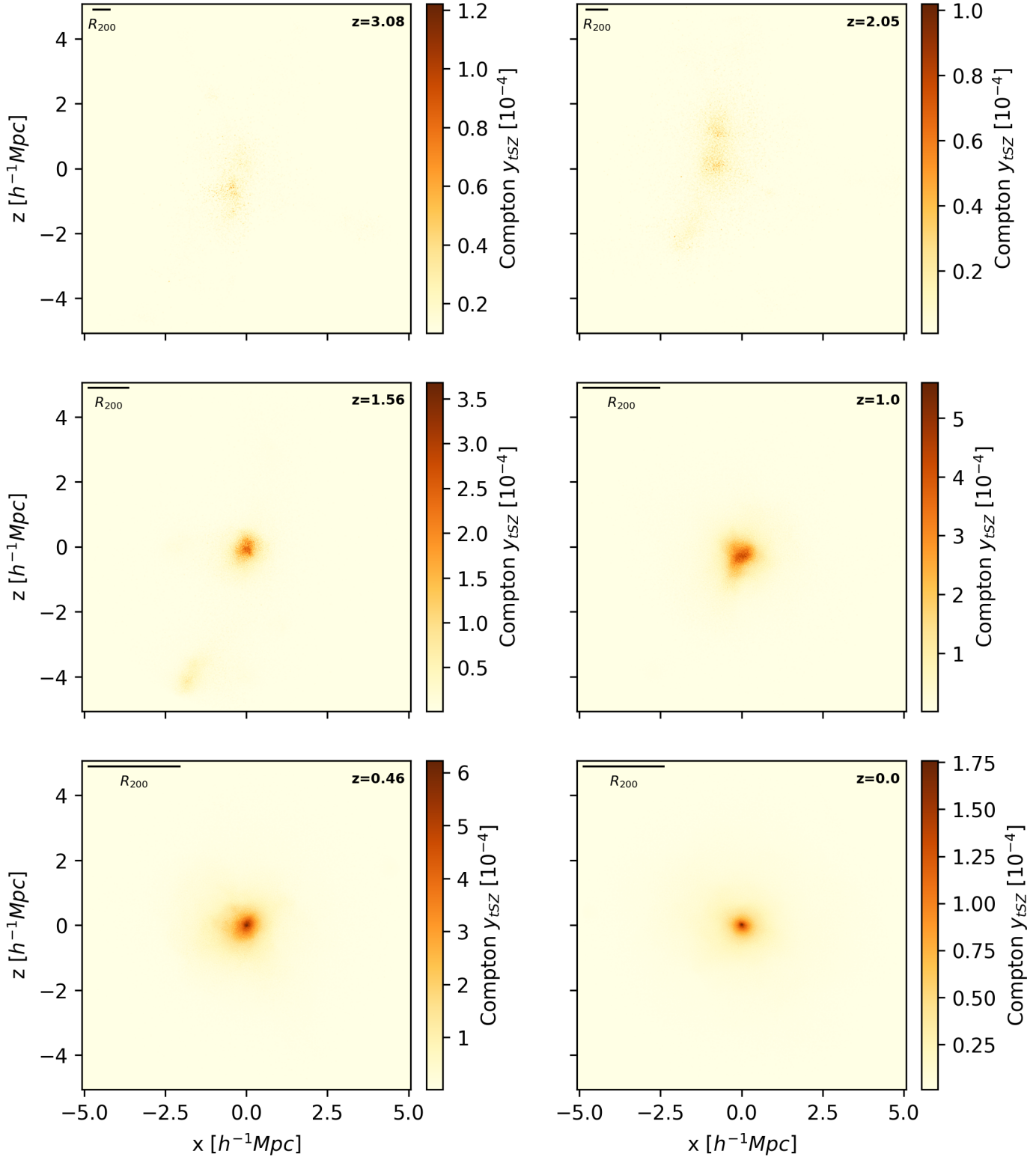


FIG. 15: Thermal SZ map of MACSIS halo 0 at $z = 0.0, 0.46, 1.0, 1.56, 2.05, 3.0$, displayed with a field of view of $2R_{200}$ of the cluster at $z = 0$. The scale bar at the top left corner shows the R_{200} of the dark matter halo, and the redshift is displayed at the top right. The map is of the thermal Compton parameter y_{tSZ} , equation 19. A Gaussian interpolation is used.

VI. CONCLUSION

This paper is a continuation of previous work, [Cooper et al. \(2022\)](#), further investigating groups, clusters, and massive clusters from the MACSIS N-body hydrodynamical simulation produced by [Barnes, Kay, et al. \(2016\)](#). The first objective was to analyse the substructure beyond the FoF haloes using the SUBFIND algorithm.

- A successful method of calculating M_{200} and R_{200} for subhaloes was implemented. Cross-checking background haloes with known FoF haloes yielded values within two decimal places.
- Selection cuts were placed to reduce the number of variables that could have negatively influenced the virial mass and radius calculation, before appending them to the preliminary FoF catalogue.
- The number of valid subhaloes resolved at $z = 0$ doubled the preliminary FoF catalogue. The fraction of valid subhaloes to FoF haloes decreased with redshift.
- The baryon fraction of subhaloes was calculated within each subhalo R_{200} and then compared to similar mass FoF haloes from previous work. The subhaloes followed the FoF halo trend of increasing baryon fraction with virial mass. However, some over-calculating of the subhalo baryon fraction is present. This could be due to the overlapping of unresolved structures.

There is an abundance of missing substructures, especially at $z = 0$, if only the FoF algorithm is applied. The properties of subhaloes match closely to that of FoF haloes. However, stricter selection criteria could be used to reduce the number of outlier subhaloes before using them for proper analysis.

The primary objective of this paper was to calculate ICM radial profiles for three mass bins representing groups, clusters and massive clusters (Table I) across a range of redshift to investigate the effect mass has on gravitational and non-gravitational processes and on self-similar evolution. Only hot gas particles ($T \geq 10^6 K$) were selected to represent the hot X-ray emitting ICM to compare to X-ray observations.

- ICM median density profiles revealed remarkable self-similarity for clusters and massive clusters across the entire probed radial and redshift range. However, the lower mass groups could not suppress the increase of feedback, such as accretion shocks, with the redshift decrease. Therefore, self-similar behaviour is not observed until the virial

radius, where gravitational processes dominate. X-ray observations and other simulations agreed closely with our results.

- ICM median temperature profiles reveal a peak that occurs at a lower radius for decreasing mass and redshift. This is due to radiative cooling and feedback blowing out gas at the core. Only massive clusters show some evidence of self-similar evolution at low radii $R/R_{200} \leq 0.3$, which after the redshift evolution of temperature increases matching groups and clusters. Observations and simulations replicated the temperature peaks and overall loosely coordinated with the evolution we saw.
- The median thermal pressure is a direct combination of the other two profiles. Again, the cluster shows the most evidence of self-similarity, with it slowly departing at the virial radius. The cluster bin exhibits a short region of self-similar behaviour $0.2 \leq R/R_{200} \leq 0.7$. Groups show a unique property of the redshift evolution, flipping at just below the virial radius. This could be the point at which gravitational physics starts to dominate the feedback processes. At $z = 0$ our pressure profile shape agreed with X-ray observations but not during redshift evolution; however, other simulations correlated more to our profiles.
- A case study of MACSIS halo 1 found a high-temperature shock front in between two clusters beginning to merge. This heats up and disturbs the ICM causing a negative effect when observing self-similar behaviour due to the affected temperature profile gradient. This is in strong agreement with observations and other simulations.

Overall the most dominant trend is the increase of self-similar evolution with the virial mass of a dark matter halo. Lower mass groups are most affected by the increased feedback processes at the core at lower redshift, causing a deviation away from self-similar behaviour. Overall, around the core radius was where our simulated profiles deviated from observational results the most. This is due to some unsimulated physics between the interaction of the feedback from the core and the ICM ([McDonald, Allen, et al. 2017](#)).

Lastly, the thermal SZ effect produced observationally realistic maps of individual clusters at high redshifts. They loosely match other simulation SZ cluster maps and need some more investigation.

VII. FUTURE WORK

The hydrostatic equilibrium mass estimation was mentioned a few times in this paper; in the future, we could calculate

the hydrostatic equilibrium mass bias using the gradient of the density and temperature profiles. We could investigate the change in bias due to the total dark matter halo mass. Furthermore, the mass can be estimated using the SZ effect using the thermal pressure profile gradient of clusters. The two could be compared.

The non-thermal pressure is a logical step in creating more profiles. This could model the bulk and turbulent motions of the ICM and provide more useful analysis to understand the processes that occur in a cluster.

Now we have built the foundation for SZ maps, we can further reproduce what a real telescope would see using convolution and point-spread functions.

REFERENCES

- M. Arnaud et al., “The universal galaxy cluster pressure profile from a representative sample of nearby systems (REXCESS) and the Y_{SZ} - M_{500} relation”, [517, A92, A92 \(2010\)](#).
- J. S. Bagla, “TreePM: a code for cosmological n-body simulations”, [Journal of Astrophysics and Astronomy 23, 185–196 \(2002\)](#).
- D. J. Barnes, R. Kannan, et al., “Enhancing AGN efficiency and cool-core formation with anisotropic thermal conduction”, [Monthly Notices of the Royal Astronomical Society 488, 3003–3013 \(2019\)](#).
- D. J. Barnes, S. T. Kay, et al., “The redshift evolution of massive galaxy clusters in the MACSIS simulations”, [Monthly Notices of the Royal Astronomical Society 465, 213–233 \(2016\)](#).
- N. Battaglia et al., “ON THE CLUSTER PHYSICS OF SUNYAEV-ZEL'DOVICH AND X-RAY SURVEYS. i. THE INFLUENCE OF FEEDBACK, NON-THERMAL PRESSURE, AND CLUSTER SHAPES ON iy/i-im/iSCALING RELATIONS”, [The Astrophysical Journal 758, 74 \(2012\)](#).
- H. Bourdin et al., “SHOCK HEATING OF THE MERGING GALAXY CLUSTER a521”, [The Astrophysical Journal 764, 82 \(2013\)](#).
- R. G. Bower, “The entropy-driven X-ray evolution of galaxy clusters”, [Monthly Notices of the Royal Astronomical Society 288, 355–364 \(1997\)](#).
- J. E. Carlstrom, G. P. Holder, and E. D. Reese, “Cosmology with the sunyaev-zel'dovich effect”, [Annual Review of Astronomy and Astrophysics 40, 643–680 \(2002\)](#).
- L. Castiblanco, R. Gannouji, and C. Stahl, *Large scale structures: from inflation to today: a brief report*, 2019.
- A. L. Coil, “The large-scale structure of the universe”, in [Planets, stars and stellar systems](#) (Springer Netherlands, 2013), pp. 387–421.
- P. Coles and F. Lucchin, *Cosmology: The Origin and Evolution of Cosmic Structure, Second Edition* (2002).
- M. Colless et al., “The 2df galaxy redshift survey: spectra and redshifts”, [Monthly Notices of the Royal Astronomical Society 328, 1039–1063 \(2001\)](#).
- W. T. Cooper and A. Callaghan, “Redshift evolution of baryon fraction and formation of massive galaxy clusters using macsis simulations”, 2022.
- M. Davis et al., “The evolution of large-scale structure in a universe dominated by cold dark matter”, [Astrophys. J. 292, 371–394 \(1985\)](#).
- S. De Grandi and S. Molendi, “Temperature Profiles of Nearby Clusters of Galaxies”, [Astrophys. J. 567, 163–177 \(2002\)](#).
- M. Dickinson et al., *Observing galaxy evolution in the context of large-scale structure*, 2019.
- J. Diemand and B. Moore, “The structure and evolution of cold dark matter halos”, [Advanced Science Letters 4, 297–310 \(2011\)](#).
- J. Diemand and B. Moore, “The structure and evolution of cold dark matter halos”, [Advanced Science Letters 4, 297–310 \(2011\)](#).
- K. Dolag et al., “Substructures in hydrodynamical cluster simulations”, [399, 497–514 \(2009\)](#).
- A. Dressler and S. A. Shectman, “Evidence for Substructure in Rich Clusters of Galaxies from Radial-Velocity Measurements”, [95, 985 \(1988\)](#).
- G. F. R. Ellis, *Issues in the philosophy of cosmology*, 2006.
- A. E. Evrard, C. A. Metzler, and J. F. Navarro, “Mass Estimates of X-Ray Clusters”, [Astrophys. J. 469, 494 \(1996\)](#).
- D. J. Fixsen, “THE TEMPERATURE OF THE COSMIC MICROWAVE BACKGROUND”, [The Astrophysical Journal 707, 916–920 \(2009\)](#).
- A. Huss, B. Jain, and M. Steinmetz, “The formation and evolution of clusters of galaxies in different cosmogonies”, [Monthly Notices of the Royal Astronomical Society 308, 1011–1031 \(1999\)](#).
- N. Kaiser, “Evolution and clustering of rich clusters”, [Monthly Notices of the Royal Astronomical Society 222, 323–345 \(1986\)](#).
- N. Katz and S. D. M. White, “Hierarchical Galaxy Formation: Overmerging and the Formation of an X-Ray Cluster”, [Astrophys. J. 412, 455 \(1993\)](#).
- S. T. Kay et al., “Sunyaev–Zel’dovich clusters in Millennium gas simulations”, [Monthly Notices of the Royal Astronomical Society 422, 1999–2023 \(2012\)](#).
- E. T. Lau et al., “MASS ACCRETION AND ITS EFFECTS ON THE SELF-SIMILARITY OF GAS PROFILES IN THE OUT-SKIRTS OF GALAXY CLUSTERS”, [The Astrophysical Journal 806, 68 \(2015\)](#).
- A. R. Liddle and D. H. Lyth, *Cosmological Inflation and Large-Scale Structure* (2000).

- B. J. Maughan et al., “Self-similar scaling and evolution in the galaxy cluster X-ray luminosity–temperature relation”, *Monthly Notices of the Royal Astronomical Society* **421**, 1583–1602 (2012).
- M. McDonald, S. W. Allen, et al., “The Remarkable Similarity of Massive Galaxy Clusters from $z \sim 0$ to $z \sim 1.9$ ”, *Astrophys. J.* **843**, 28, 28 (2017).
- M. McDonald, B. A. Benson, et al., “THE REDSHIFT EVOLUTION OF THE MEAN TEMPERATURE, PRESSURE, AND ENTROPY PROFILES IN 80 SPT-SELECTED GALAXY CLUSTERS”, *The Astrophysical Journal* **794**, 67 (2014).
- H. Mo, F. van den Bosch, and S. White, *Galaxy formation and evolution* (Cambridge University Press, 2010).
- H. Mo, v. F. C., and S. White, *Galaxy Formation and Evolution* (2010).
- P. M. Motl et al., “The integrated sunyaev-zeldovich effect as a superior method for measuring the mass of clusters of galaxies”, *The Astrophysical Journal* **623**, L63 (2005).
- M. T. Moura, R. E. G. Machado, and R. Monteiro-Oliveira, “Simulations of the merging galaxy cluster abell 2034: what determines the level of separation between gas and dark matter”, *Monthly Notices of the Royal Astronomical Society* **500**, 1858–1869 (2020).
- T. Mroczkowski et al., “Astrophysics with the spatially and spectrally resolved sunyaev-zeldovich effects”, *Space Science Reviews* **215**, 10.1007/s11214-019-0581-2 (2019).
- R. Mushotzky, “X-ray emission from clusters and groups of galaxies”, *Proceedings of the National Academy of Sciences* **95**, 72–77 (1998).
- P. Natarajan and V. Springel, “Abundance of substructure in clusters of galaxies”, *The Astrophysical Journal* **617**, L13–L16 (2004).
- F. Pearce, “Simulations of galaxy clusters”, (2020).
- F. A. Pearce et al., “Hydrostatic mass estimates of massive galaxy clusters: a study with varying hydrodynamics flavours and non-thermal pressure support”, *Monthly Notices of the Royal Astronomical Society* **491**, 1622–1642 (2019).
- Planck Collaboration et al., “Planck 2013 results. XVI. Cosmological parameters”, *571*, A16, A16 (2014).
- S. Planelles, D. Fabjan, et al., “Pressure of the hot gas in simulations of galaxy clusters”, *Monthly Notices of the Royal Astronomical Society* **467**, 3827–3847 (2017).
- S. Planelles, D. R. G. Schleicher, and A. M. Bykov, “Large-scale structure formation: from the first non-linear objects to massive galaxy clusters”, *Space Science Reviews* **188**, 93–139 (2014).
- Poudel, A. et al., “The effect of cosmic web filaments on the properties of groups and their central galaxies”, *A&A* **597**, A86 (2017).
- Y. Rephaeli, “Comptonization Of The Cosmic Microwave Background: The Sunyaev-Zeldovich Effect”, *33*, 541–580 (1995).
- C. L. Sarazin, “X-ray emission from clusters of galaxies”, *Rev. Mod. Phys.* **58**, 1–115 (1986).
- C. J. Short et al., “The evolution of galaxy cluster X-ray scaling relations”, *408*, 2213–2233 (2010).
- D. Sijacki et al., “A unified model for AGN feedback in cosmological simulations of structure formation”, *Monthly Notices of the Royal Astronomical Society* **380**, 877–900 (2007).
- A. C. da Silva et al., “Hydrodynamical simulations of the Sunyaev-Zel'dovich effect”, *Monthly Notices of the Royal Astronomical Society* **317**, 37–44 (2000).
- V. Springel, “The cosmological simulation code gadget-2”, *Monthly Notices of the Royal Astronomical Society* **364**, 1105–1134 (2005).
- V. Springel, S. D. M. White, et al., “Populating a cluster of galaxies – I. Results at $z = 0$ ”, *Monthly Notices of the Royal Astronomical Society* **328**, 726–750 (2001).
- V. Springel, N. Yoshida, and S. D. M. White, “GADGET: a code for collisionless and gasdynamical cosmological simulations”, *6*, 79–117 (2001).
- R. A. Sunyaev and Y. B. Zel'dovich, “Microwave background radiation as a probe of the contemporary structure and history of the universe”, *Annual Review of Astronomy and Astrophysics* **18**, 537–560 (1980).
- R. A. Sunyaev and Y. B. Zeldovich, “The Spectrum of Primordial Radiation, its Distortions and their Significance”, *Comments on Astrophysics and Space Physics* **2**, 66 (1970).
- J. E. Taylor, “Dark matter halos from the inside out”, *Advances in Astronomy* **2011**, 1–17 (2011).
- G. Tormen, F. R. Bouchet, and S. D. M. White, “The structure and dynamical evolution of dark matter haloes”, *Monthly Notices of the Royal Astronomical Society* **286**, 865–884 (1997).
- R. B. Tully et al., “The laniakea supercluster of galaxies”, *Nature* **513**, 71–73 (2014).
- A. A. Vikhlinin et al., “Clusters of galaxies”, *Physics-Uspekhi* **57**, 317 (2014).
- A. Vikhlinin et al., “Chandra Sample of Nearby Relaxed Galaxy Clusters: Mass, Gas Fraction, and Mass-Temperature Relation”, *Astrophys. J.* **640**, 691–709 (2006).
- S. D. M. White and M. J. Rees, “Core condensation in heavy halos: a two-stage theory for galaxy formation and clustering.”, *183*, 341–358 (1978).
- E. L. Wright, *Sunyaev-zeldovich spectrum*, From: <https://astro.ucla.edu/~wright/intro.html>, 2013.

This document has been typeset from a L^AT_EX file prepared by the author.

Appendix A: Subhaloe Virial Parameters

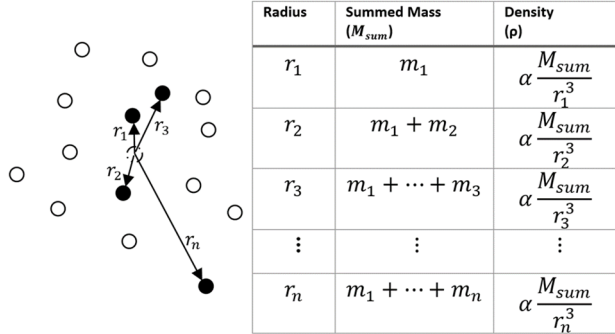


FIG. 16: Schematic of the method used to calculate the virial mass and radius in section III A. r_1 represents the smallest distance to the centre of the potential (most bound particle), indicated by the dashed-dotted ring in the middle, and r_n is the distance to the furthest particle. The table shows the distance to bound particles in ascending order. The mass at every radius is the summed mass of that particle and all other particles closer than it. The density is then calculated as shown by the right column for every row in the table. The α is a constant. The row in the table that is closest to the critical density (equation 3) means the particle radius and summed mass are the virial radius and mass, respectively, as in equation 5